

Dissipation and fluctuations of CMOS ring oscillators close to criticality

Ashwin Gopal,¹ Massimiliano Esposito,¹ and Jan Meibohm²

¹*Complex Systems and Statistical Mechanics, Department of Physics and Materials Science, University of Luxembourg, 30 Avenue des Hauts-Fourneaux, L-4362 Esch-sur-Alzette, Luxembourg*

²*Theoretical Physics Unit, Institute for Physics and Astronomy, Technische Universität Berlin, Hardenbergstraße 36, 10623 Berlin, Germany*

We analyze a thermodynamically consistent model of CMOS-based ring oscillators near the onset of coherent voltage oscillations. For driving voltages close to the critical value, we derive the normal form of the Hopf bifurcation that underlies the oscillation transition in the thermodynamic limit. Using this normal form, we determine the phase and amplitude dynamics, and demonstrate that entropy dissipation decreases in the oscillating state for ring oscillators with more than three inverters. These findings culminate in a stability-dissipation relation, which links the observed decrease in dissipation to an increase in the local stability of the oscillating state. Next, we characterize finite-size fluctuations of the amplitude and phase near the critical voltage, using a stochastic version of the normal form. We demonstrate that close to the transition, finite-size fluctuations remain important at arbitrary system size, introducing oscillations even below the critical voltage. We further show that these noise-induced oscillations have an anomalously short decoherence time that scales sub-linearly with the system-size, in contrast to the behavior far from criticality.

I. INTRODUCTION

Self-sustained oscillations are paradigmatic phenomena in non-equilibrium physics, manifested across systems ranging from biochemical [1, 2], and electronic clocks [3, 4], to nonlinear optics [5, 6] and hydrodynamics [7]. Driven far from equilibrium, these systems undergo a qualitative change from stationary states, whose probability distributions are concentrated near stable fixed points, to oscillating states, concentrated around the orbits of stable limit cycles. In the thermodynamic limit, this dynamical transition is sharp and well-described by deterministic bifurcation theory [3, 8, 9]. Recent work has revealed relationships between dynamical stability and dissipation, close to criticality at the deterministic level [10, 11]. However, on the mesoscopic scale, where the magnitude of thermal fluctuations is comparable to the size of the order parameter, the distinction between deterministic dynamics and thermal noise blurs. At this “edge of instability,” emerges a regime of rich physical interplay, with complex dynamical and thermodynamical behaviors [12–16].

Complementary metal-oxide-semiconductor (CMOS) circuits [17] provide a practical platform to investigate this interplay between deterministic and stochastic dynamics, and its thermodynamic implications [18–21]. As CMOS transistors scale down, with smaller physical dimensions and lower supply voltage, various sources of physical noise become relevant to the signal. This is particularly acute in ultra-low-power applications [22, 23] and neuromorphic computing [24–26], where circuits often operate in the subthreshold regime with supply voltages approaching the thermal voltage. Among the diverse digital, analog, and mixed-signal components built from CMOS transistors, ring oscillators constitute a fundamental building block for timing, frequency generation, and signal processing. Their minimal design, high tunability, and compatibility with standard fabri-

cation processes make them indispensable in both high-performance and ultra-low-power applications [27].

Ring oscillators are electronic devices composed of an odd number of inverters connected in a loop [28, 29]; see Fig. 1. Their output voltages oscillate because of an inherent instability in the circuit’s logical states. This instability drives the loop into self-sustained oscillations, whose frequency is determined by the number of inverters and the propagation delay between them. This delay, in turn, is controlled by the voltage across the inverters, so ring oscillators are highly tunable and therefore commonly serve as voltage-controlled oscillators in phase-locked loops [28, 29]. Their tunability and simplicity make ring oscillators essential components in CMOS technology, particularly in timing and frequency-synthesis applications.

Current fluctuations in the transistors – thermal or flicker – induce random variations of the oscillation phase producing phase noise, and causing ring oscillators to lose coherence over time, manifested as jitter [30]. Although detrimental in clocking contexts, phase noise can be exploited to design “true random number generators” [31–33]. Unlike pseudo-random number generators, these devices rely on inherently noisy physical processes and are used in secure communication and cryptographic systems where unpredictability is essential [34]. True randomness can be generated by combining the uncertainties of multiple ring oscillators to produce a bit stream at specified sampling intervals. In this way, amplified phase noise is harnessed to construct efficient true random number generators even in the subthreshold regime of ultra-low power [35, 36].

In this paper, we analyze a thermodynamically consistent model of ring oscillators near the critical voltage, at which small-amplitude oscillations emerge. We derive the normal form for the Hopf bifurcation of the dominant oscillating mode that underlies the transition, enabling us to determine the amplitude and frequency of oscillations

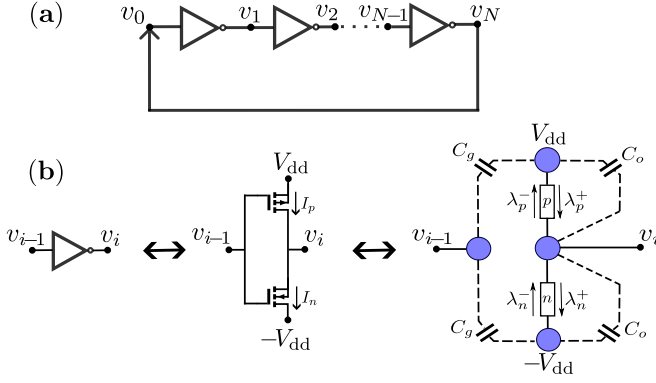


FIG. 1. (a) Logical representation of a ring oscillator as an odd number N of inverters (NOT gates) connected in a loop, i.e. $v_N = v_0$. (b) CMOS implementation of the NOT gate (inverter) using pMOS and nMOS transistors, and a bi-Poissonian charge-transport model including the gate-body C_g and drain-source C_o capacitances [18].

close to onset. Using the framework of stochastic thermodynamics [37–39], we show that entropy production decreases in the oscillatory state for ring oscillators with more than three inverters. Based on these findings, we derive a stability-dissipation relation, similar to that in Refs. [10, 11], linking the reduced entropy production to the enhanced local stability of the oscillating state.

We then characterize phase noise near the critical voltage, where conventional large-amplitude approaches [40–42] become inaccurate. Our analysis is based on a “stochastic normal form” [43] that incorporates the leading noise-induced effects. Close to the oscillation transition, such effects remain relevant, regardless of the large system size. In particular, they generate noise-induced oscillations even below the critical voltage. In contrast to large-amplitude oscillations [42, 44], these oscillations exhibit unusually strong decoherence with an anomalously short coherence time. This property may indicate that noise-induced oscillations could be especially well suited for generating high-rate, statistically independent true random numbers.

The paper is organized as follows. In Sec. II we introduce the thermodynamically consistent formulation of electric circuits of Ref. [18] and describe our model. In Sec. III we analyze the thermodynamic limit, identify the equilibrium fixed point and its instability at the critical voltage, and derive the Hopf normal form that characterizes small-amplitude oscillations. We then discuss the stability and thermodynamics of the deterministic system. Section IV addresses finite-size fluctuations: Here, we analyze the stochastic normal form, noise-induced oscillations, and the resulting (short) decoherence time. Finally, we present our conclusions in Sec. V.

II. MODEL

We consider a CMOS-based ring oscillator composed of (odd) N inverters [see Fig. 1(a)], in contact with a heat bath at temperature T . Each inverter is composed of two metal-oxide-semiconductor field-effect transistors (MOSFETs) [Fig. 1(b), center], one n -doped (“nMOS”, bottom) and one p -doped (“pMOS”, top). The heat bath induces finite-temperature voltage fluctuations in the system. In order to consistently describe them, we need to account for the voltage fluctuations that arise from all $2N$ MOSFETs in the circuit.

Using the formalism in Ref. [18], we model MOSFETs as conduction channels subject to thermal noise. We consider the subthreshold regime in which voltage changes across the transistors are caused by single-electron transitions through the conduction channels. Hence, electron transitions through the nMOS and pMOS transistors of the i th inverter are treated as bidirectional Poisson processes, characterized by a forward (+) and a backward (−) transition rate $\lambda_{i\pm}^{n/p}(v_{i-1}, v_i)$. Here, v_i denotes the output voltage of the i th inverter.

The inverters are connected in a loop, see Fig. 1(a), so the input of the first inverter is the output of the last inverter, i.e. $v_N = v_0$ and, more generally, $v_i = v_{i \bmod N}$. Because MOSFETs typically have insulating gate terminals, changes in the i th component v_i of the output voltage are only due to charge transitions in the transistors of the i th inverter.

The allowed transitions in the voltage vector $\mathbf{v} = (v_0, \dots, v_{N-1})^T$ are given by

$$\mathbf{v} \rightarrow \mathbf{v} + \Delta_{i\pm}^{p/n} v_e, \quad (1)$$

with

$$(\Delta_{i\pm}^p)^m = \pm \delta_{im} \quad \text{and} \quad (\Delta_{i\pm}^n)^m = \mp \delta_{im}, \quad (2)$$

where δ_{mn} is the Kronecker delta and $v_e \equiv q_e/C$ represents the elementary change of the output voltage due to a single charge transfer. Furthermore, $C = 2(C_o + C_g)$ describes the effective capacitance at the output node with contributions from the gate-body capacitance C_g and additional output capacitance C_o caused by the transistors connected to the node.

The current I_p through a pMOS transistor as a function of the input V_{in} , output V_{out} and driving voltages V_{dd} is given by [18]

$$I_p(V_{in}, V_{out}; V_{dd}) = I_0 e^{(V_{dd} - V_{in} - V_{th})/V_T} \left[1 - e^{-(V_{dd} - V_{out})/V_T} \right], \quad (3)$$

where V_{th} denotes the threshold voltage and I_0 is the characteristic current, which are parameters determined by the transistor specifications.

We consider CMOS devices with symmetric transistor parameters for pMOS and nMOS transistors and further apply the symmetric powering voltages V_{dd} and $-V_{dd}$,

respectively. In such a setup, the current I_n through an nMOS transistor is obtained by inverting the input and output voltages in Eq. (3), i.e.,

$$I_n(V_{\text{in}}, V_{\text{out}}; V_{\text{dd}}) = I_p(-V_{\text{in}}, -V_{\text{out}}; V_{\text{dd}}). \quad (4)$$

The deterministic I - V characteristics (3) and (4) together with the local detailed balance condition, required for thermodynamic consistency according to stochastic thermodynamics [37–39], uniquely determine the transition rates $\lambda_{i\pm}^{\text{n/p}}(v_{i-1}, v_i)$ for all transistors [18]. The transition rates for the i th pMOS transistor of the ring oscillator can be written as

$$\begin{aligned} \lambda_{i+}^{\text{p}}(\mathbf{v}) &= \frac{\Omega}{\tau_0} e^{(V_{\text{dd}} - v_{i-1})/V_{\text{T}}}, \\ \lambda_{i-}^{\text{p}}(\mathbf{v}) &= \frac{\Omega}{\tau_0} e^{(v_i - v_{i-1})/V_{\text{T}}} e^{-1/2\Omega}, \end{aligned} \quad (5)$$

where we have defined the system size parameter $\Omega = V_{\text{T}}/v_e = k_{\text{B}}TC/q_e^2$ and the characteristic timescale $\tau_0 = [(V_{\text{T}}C)/I_0]e^{V_{\text{th}}/V_{\text{T}}}$ with the thermal voltage $V_{\text{T}} = k_{\text{B}}T/q_e$. The previously described symmetries between the MOSFETs imply that the transition rates for nMOS are given by

$$\lambda_{i\pm}^{\text{n}}(\mathbf{v}) = \lambda_{i\pm}^{\text{p}}(-\mathbf{v}). \quad (6)$$

Combining these ingredients, the dynamics of the probability $P(\mathbf{v}, t)$ to find the system in state \mathbf{v} at time t is given by the Master equation

$$\begin{aligned} \partial_t P(\mathbf{v}, t) &= \sum_{i=0}^{N-1} \sum_{\rho=\text{n,p}} \left\{ \lambda_{i+}^{\rho}(\mathbf{v} - v_e \Delta_{i+}^{\rho}) P(\mathbf{v} - v_e \Delta_{i+}^{\rho}, t) \right. \\ &\quad + \lambda_{i-}^{\rho}(\mathbf{v} - v_e \Delta_{i-}^{\rho}) P(\mathbf{v} - v_e \Delta_{i-}^{\rho}, t) \\ &\quad \left. - [\lambda_{i+}^{\rho}(\mathbf{v}) + \lambda_{i-}^{\rho}(\mathbf{v})] P(\mathbf{v}, t) \right\}. \end{aligned} \quad (7)$$

Figure 2 shows sample trajectories for the output voltage v_0 of a 7-stage ring oscillator for different driving voltages V_{dd} . We observe that for small V_{dd} the stochastic trajectories fluctuate incoherently around $\mathbf{v} = 0$, with small amplitudes (blue and red in Fig. 2). Upon increasing V_{dd} across a critical voltage V_{dd}^* to be determined, the oscillations become coherent and grow in amplitude (green in Fig. 2). We explain this behavior in detail in the next Sections.

III. SMALL AMPLITUDE OSCILLATIONS IN THERMODYNAMIC LIMIT

The onset of coherent oscillations upon increasing V_{dd} , observed in Fig. 2, is most conveniently described in the thermodynamic limit $\Omega \rightarrow \infty$ of large system size. Physically, this limit can be realized by simply increasing the physical dimensions of the transistor [45], so that the elementary voltage change v_e becomes negligible compared with all other voltages. Since the current flow scales with

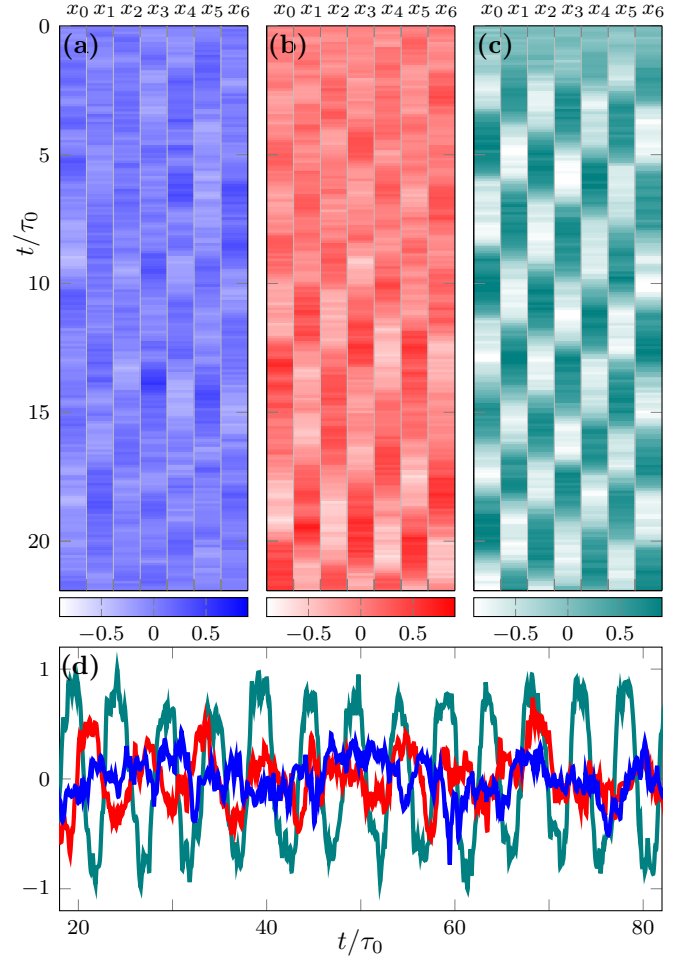


FIG. 2. Dimensionless output voltage vector $\mathbf{x} = \mathbf{v}/V_{\text{T}}$ as function of time t below and above the critical voltage $V_{\text{dd}}^*/V_{\text{T}} \approx 0.7466$ for a 7-stage ring oscillator with system size $\Omega = 10^2$. (a) \mathbf{x} as function of t for $\lambda = (V_{\text{dd}} - V_{\text{dd}}^*)/V_{\text{T}} = -0.1$ as color map. Darker colors correspond to higher voltages (b) $\lambda = 0$. (c) $\lambda = 0.2$. (d) Voltage v_0 as function of t for $\lambda = -0.1$ (blue), $\lambda = 0$ (red), and $\lambda = 0.2$ (green).

the physical dimensions of the channel, we define rescaled transition rates $\omega_{\text{n/p}}^{\pm}(\mathbf{v})$ as

$$\omega_{i\pm}^{\text{n/p}}(\mathbf{v}) \equiv \lim_{\Omega \rightarrow \infty} \frac{\lambda_{i\pm}^{\text{n/p}}(\mathbf{v})}{\Omega}. \quad (8)$$

To determine the dynamics in this limit, we expand the Master equation (7) to lowest order in Ω^{-1} to obtain

$$\partial_t P(\mathbf{v}, t) = -\nabla_{\mathbf{v}} \cdot [\mathbf{F}(\mathbf{v}) P(\mathbf{v}, t)] + \mathcal{O}(1/\Omega), \quad (9)$$

where we have identified the deterministic drift

$$\begin{aligned} \mathbf{F}(\mathbf{v}) &= \sum_{i=0}^{N-1} \sum_{\rho=\text{n,p}} [\Delta_{i+}^{\rho} \omega_{i+}^{\rho}(\mathbf{v}) + \Delta_{i-}^{\rho} \omega_{i-}^{\rho}(\mathbf{v})], \\ &= \frac{2}{\tau_0} \left[\sinh \left(\frac{v_{i-1}(t) - v_i(t)}{V_{\text{T}}} \right) - e^{V_{\text{dd}}/V_{\text{T}}} \sinh \left(\frac{v_{i-1}(t)}{V_{\text{T}}} \right) \right]. \end{aligned} \quad (10)$$

Due to the absence of a diffusion term in Eq. (9), the trajectories of the output voltages v_i follow a deterministic dynamics given by

$$\frac{\dot{v}_i(t)}{V_T} = F_i(\mathbf{v}) = \tau_0^{-1} h\left(\frac{v_i}{V_T}, \frac{v_{i-1}}{V_T}\right), \quad (11)$$

where $\dot{v}_i = \frac{d}{dt}v_i$ denotes a time derivative and the function

$$h(x, y) = 2 \left[\sinh(y - x) - e^{V_{dd}/V_T} \sinh(y) \right], \quad (12)$$

is identical for all i . In what follows, we discuss the basic properties of Eq. (11).

A. Symmetry

As one can anticipate by considering Fig. 1, ring oscillators composed of identical inverters are invariant under cyclic permutations of the inverters. This symmetry directly carries over to the output voltages \mathbf{v} , and is thus reflected in the dynamics (11).

For the ring oscillator, we define the symmetry operation γ as $\gamma = \mathcal{R}^n$ for some integer $n \geq 0$, where the generator \mathcal{R} cyclically permutes the components of \mathbf{v} by one, i.e.,

$$(v_0, v_1, \dots, v_{N-1})^T \xrightarrow{\mathcal{R}} (v_{N-1}, v_0, v_1, \dots, v_{N-2})^T. \quad (13)$$

Symmetry under the action of γ implies that the macroscopic dynamics of the system, described by Eq. (11), must be *equivariant* with respect to the action of γ [8], which entails that

$$\mathbf{F}(\mathbf{v}) = \gamma^{-1} \mathbf{F}(\gamma \mathbf{v}). \quad (14)$$

This property can be seen to hold true by considering the right-hand side of Eq. (11), because the function h is independent of the index i .

The cyclic permutation symmetry of inverters is a crucial property of the ring oscillator that we will use repeatedly in what follows.

B. Trivial fixed point

Since $\sinh(0) = 0$, one finds by inspection that Eq. (11) admits a trivial fixed point when all voltages vanish, i.e., $\mathbf{v}^* = (0, 0, \dots, 0)^T$. Without external drive ($V_{dd} = 0$), the device is in thermal equilibrium, so that \mathbf{v}^* must be stable. Driven devices ($V_{dd} \neq 0$), by contrast, are intrinsically out of equilibrium, so \mathbf{v}^* may become unstable, giving rise to dynamic behavior. Generally, the stability of \mathbf{v}^* is governed by the eigenvalues of the stability matrix \mathbb{M} with elements

$$M_{ij} = V_T \frac{\partial F_i(\mathbf{v})}{\partial v_j} \bigg|_{\mathbf{v}=\mathbf{v}^*} = \tau_0^{-1} (h_{10} \delta_{ij} + h_{01} \delta_{i-1j}), \quad (15)$$

where all indices are understood modulo N and where we defined

$$h_{ij} = \partial_x^i \partial_y^j h(x, y) \big|_{x=y=0}, \quad (16)$$

so that

$$h_{10} = -2, \quad h_{01} = -2(e^{V_{dd}/V_T} - 1). \quad (17)$$

The fixed point \mathbf{v}^* is considered stable when all eigenvalues of \mathbb{M} have a negative real part. If one or more of the eigenvalues have positive real parts, by contrast, perturbations along the corresponding eigendirections grow over time, and the fixed point is said to be unstable. To determine the conditions under which \mathbf{v}^* is stable, we need to diagonalize the stability matrix \mathbb{M} .

From Eq. (15) we observe that \mathbb{M} is a circulant matrix [46], which means that \mathbb{M} commutes with γ ,

$$\gamma \mathbb{M} = \mathbb{M} \gamma. \quad (18)$$

This commutation relation, in turn, is a consequence of the equivariance property (14) and thus of the symmetry of the ring oscillator. An important consequence of Eq. (18) is that the eigenvectors of \mathbb{M} are discrete Fourier modes

$$\hat{\mathbf{v}}_k = \left(1, e^{\frac{i2\pi k}{N}}, e^{\frac{i4\pi k}{N}}, \dots, e^{\frac{i2\pi k(N-1)}{N}} \right)^T \quad (19)$$

for $k = 0, 1, \dots, N-1$ and that \mathbb{M} is diagonalized by the discrete Fourier transform \mathbb{F} , i.e.,

$$\mathbb{D} = \mathbb{F} \mathbb{M} \mathbb{F}^{-1}, \quad (20)$$

where \mathbb{D} is the diagonal form of \mathbb{M} and \mathbb{F} and its inverse have the elements

$$F_{kn} = e^{\frac{i2\pi kn}{N}}, \quad F_{nk}^{-1} = \frac{1}{N} e^{-\frac{i2\pi kn}{N}}. \quad (21)$$

The eigenvalues $\mathcal{D}_k = \mathbb{D}_{kk}$ of \mathbb{M} are then obtained as $\mathcal{D}_k = \mu_k + i\omega_k$, where

$$\begin{aligned} \mu_k &= h_{10} + h_{01} \cos\left(\frac{2\pi k}{N}\right), \\ &= -2 \left[1 + (e^{V_{dd}/V_T} - 1) \cos\left(\frac{2\pi k}{N}\right) \right], \end{aligned} \quad (22)$$

and

$$\omega_k = h_{01} \sin\left(\frac{2\pi k}{N}\right) = -2(e^{V_{dd}/V_T} - 1) \sin\left(\frac{2\pi k}{N}\right). \quad (23)$$

In the undriven (equilibrium) case $V_{dd} = 0$, all eigenvalues of \mathbb{M} are negative, implying that \mathbf{v}^* is stable, as previously anticipated. However, as the voltage V_{dd} increases, there is a change in sign of μ_{k^*} , i.e., the fixed point becomes unstable, for the pair of Fourier modes $\pm k^*$ (modulo N) with $k^* = (N-1)/2$ and $-k^* = (N+1)/2$. At the bifurcation where $\mu_{\pm k^*} = 0$, the imaginary parts $\omega_{\pm k^*} = \pm \omega_{k^*}$ of the eigenvalues remain finite, which indicates a Hopf

bifurcation [3, 9]. The critical voltage $V_{\text{dd}}^*/V_{\text{T}}$ at which this bifurcation occurs can be expressed as

$$\frac{V_{\text{dd}}^*}{V_{\text{T}}} = \log \left[1 + \sec \left(\frac{\pi}{N} \right) \right], \quad (24)$$

for odd N , where $\sec(x) = 1/\cos(x)$. As $\sec(\pi/N)$ decreases with increasing number of inverters for $N \geq 3$, the critical voltage V_{dd}^* decreases with increasing N .

If V_{dd} is increased even further, more pairs of Fourier modes $\pm k_m^* = [N \mp (2m-1)]/2$, where $m = 2, \dots, (N-1)/2$, become unstable through additional Hopf bifurcations. However, since these bifurcations emerge from the already unstable fixed point \mathbf{v}^* , they are much less relevant to the global dynamics than the primary bifurcation of the k^* mode at V_{dd}^* in Eq. (24), which renders the stable fixed point at \mathbf{v}^* unstable. We therefore call k^* the critical Fourier mode. Once this primary bifurcation has occurred, the system is driven away from \mathbf{v}^* and towards other stable states in the long-time limit. The occurrence of stable states in the vicinity of the bifurcation is determined by the bifurcation's normal form, which we analyze in the following.

C. Hopf normal form

In order to determine the behavior of the system close to the bifurcation at V_{dd}^* , we consider small variations $\mathbf{x} = (\mathbf{v} - \mathbf{v}^*)/V_{\text{T}}$ around the fixed point \mathbf{v}^* with $|\mathbf{x}| \ll 1$. To this end, we Taylor-expand the deterministic dynamics Eq. (11) up to $\mathcal{O}(\mathbf{x}^3)$, obtaining

$$\begin{aligned} \tau_0 \dot{x}_i &\sim h_{10}x_i + h_{01}x_{i-1} + \frac{1}{6} (h_{30}x_i^3 + 3h_{21}x_i^2x_{i-1} \\ &\quad + 3h_{12}x_ix_{i-1}^2 + h_{03}x_{i-1}^3), \\ &= -2[x_i + (e^{V_{\text{dd}}/V_{\text{T}}} - 1)x_{i-1}] + x_i^2x_{i-1} - x_ix_{i-1}^2 \\ &\quad - \frac{1}{3}[x_i^3 + (e^{V_{\text{dd}}/V_{\text{T}}} - 1)x_{i-1}^3], \end{aligned} \quad (25)$$

where we have neglected $\mathcal{O}(x^4)$ terms and used $h_{20} = h_{11} = h_{02} = 0$, $h_{30} = h_{12} = -h_{21} = -2$, and $h_{03} = -2(e^{V_{\text{dd}}/V_{\text{T}}} - 1)$. We observe that all quadratic terms in the expansion in Eq. (25) vanish. This property of the model makes the calculations that follow significantly simpler because it will allow us to simply read off the Hopf normal form from the Fourier-transformed dynamics without explicit calculations.

To get there, we decompose the variations \mathbf{x} into their discrete Fourier modes $\hat{\mathbf{x}} = (\hat{x}_0, \hat{x}_1, \dots, \hat{x}_{N-1})^T$ by $\hat{\mathbf{x}} = \mathbb{F} \mathbf{x}$ using the matrix \mathbb{F} in Eq. (21). We obtain

$$\begin{aligned} \tau_0 \dot{\hat{x}}_k &\sim (\mu_k + i\omega_k)\hat{x}_k + \frac{1}{N^2} \sum_{k', k''=0}^{N-1} \left[\frac{1}{6}(\mu_k + i\omega_k) \right. \\ &\quad \left. + e^{\frac{i2\pi k'}{N}} \left(1 - e^{\frac{i2\pi k''}{N}} \right) \right] \hat{x}_{k'} \hat{x}_{k''} \hat{x}_{k-k'-k''}. \end{aligned} \quad (26)$$

Since the variations \mathbf{x} are real, the Fourier components \hat{x}_k occur in complex conjugate pairs z_k and \bar{z}_k , such that

$$z_k = \hat{x}_k, \quad \bar{z}_k = \hat{x}_{-k}. \quad (27)$$

As we have observed in Sec. IIIB, the trivial fixed point loses its stability when increasing V_{dd} across V_{dd}^* in Eq. (24), showing characteristics of a Hopf bifurcation in the plane spanned by \hat{x}_{k^*} and \hat{x}_{-k^*} . The parametric distance from the critical voltage V_{dd}^* is conveniently measured by the bifurcation parameter

$$\lambda = \frac{V_{\text{dd}} - V_{\text{dd}}^*}{V_{\text{T}}}. \quad (28)$$

For $\lambda > 0$ close to the bifurcation, i.e., $\lambda \ll 1$, the long-term dynamics of the system are predominantly governed by the growing critical Fourier mode z_{k^*} with $k^* = (N-1)/2$, because $\mu_{k^*} > 0$. All other modes $z_{k \neq k^*}$, on the contrary, have $\mu_k < 0$, and thus decay exponentially over time, leading to $z_k = \bar{z}_k = 0$ for $k \neq k^*$ in the long-time limit. Since these non-critical modes vanish, the dynamics near the bifurcation can be effectively described by the critical Fourier mode k^* alone.

Figure 3 shows this behavior for $N = 7$, so that $k^* = 3$: The figure shows the steady-state probability density of the Fourier modes z_1, z_2 and z_3 in the complex plane below and above the critical voltage V_{dd}^* , i.e., for negative and positive λ , respectively. For $\lambda > 0$ we clearly observe the emergence of the non-vanishing critical mode z_{k^*} rotating in the $k^* = 3$ plane, while the amplitudes of all other modes remain small.

In addition to the irrelevance of the non-critical modes, the analysis of z_{k^*} is further simplified by studying the normal form of the Hopf bifurcation of z_{k^*} . This simplified form of Eq. (26) represents an equivalent description of the dynamics close to the bifurcation but contains only the essential terms. In the general case, to bring (25) into normal form, one applies a non-linear coordinate transform that removes all non-essential terms from the cubic expansion in Eq. (26) [8, 48], as done explicitly in [10, 11]. However, in the case at hand, this procedure is not necessary, because the quadratic terms in the expansion in Eq. (26) vanish identically. This implies that coordinate transforms to remove the third-order inessential terms will produce only corrections of order four and higher [8, 48], which we can safely neglect. Consequently, the Hopf normal form [9] for the bifurcation of z_{k^*} can simply be read off Eq. (26), leading us to

$$\tau_0 \dot{z}_{k^*} \sim (\mathcal{D}_{k^*} - \mathcal{C}_{k^*} |z_{k^*}|^2) z_{k^*}. \quad (29)$$

The linear term $\mathcal{D}_{k^*} = \mu_{k^*} + i\omega_{k^*}$ in Eq. (29) captures the instability of the fixed point \mathbf{v}^* , as discussed in Sec. IIIB. We expand \mathcal{D}_{k^*} to linear order in λ , to obtain

$$\mu_{k^*} = 4 \cos^2 \left(\frac{\pi}{2N} \right) \lambda + \mathcal{O}(\lambda^2), \quad (30)$$

$$\omega_{k^*} = -\tan \left(\frac{\pi}{N} \right) (2 + \mu_{k^*}) + \mathcal{O}(\lambda^2). \quad (31)$$

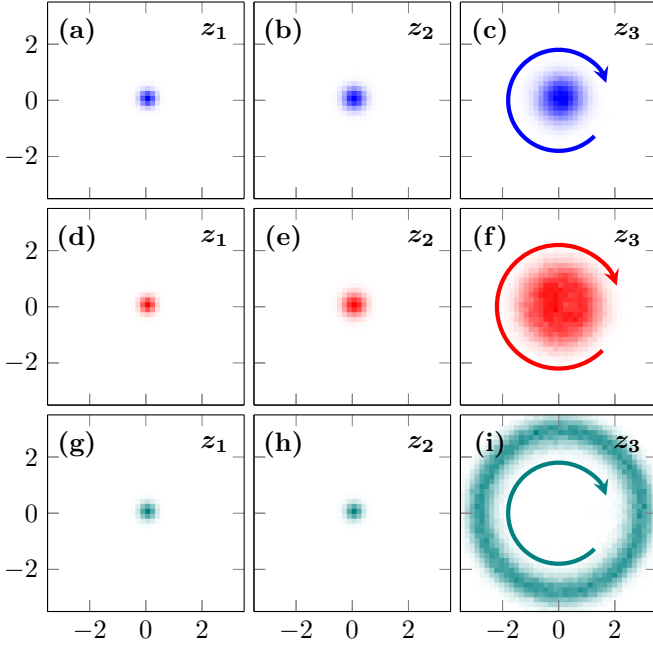


FIG. 3. Steady-state probability density of Fourier modes z_i , $i = 1, 2, 3$, for a $N = 7$ -stage ring oscillator below and above the critical voltage V_{dd}^* , obtained from Gillespie simulations [47] with $\Omega = 10^2$, averaged over 10^2 realizations and over a time interval $\Delta t \approx 100\tau_0$. The probability density is shown as a heat map in the complex plane, where the horizontal axes correspond to the real parts, the vertical axes to the imaginary parts of z_i . Darker colors indicate higher density, arrows indicate directions of rotation. (a)–(c) $\lambda = -0.1$. (d)–(f) $\lambda = 0$. (g)–(i) $\lambda = 0.2$.

The properties of small-amplitude oscillations are encoded in the cubic term in Eq. (29). We divide \mathcal{C}_{k^*} into real and imaginary parts, $\mathcal{C}_{k^*} = \mathcal{A}_{k^*} + i\mathcal{B}_{k^*}$. To leading order in λ , we find

$$\begin{aligned} \mathcal{A}_{k^*} &= \frac{2}{N^2} \cos^2\left(\frac{\pi}{2N}\right) \left[4 \cos^2\left(\frac{\pi}{2N}\right) - 1 \right] + \mathcal{O}(\lambda) \\ \mathcal{B}_{k^*} &= -\frac{1}{N^2} \left[\cos\left(\frac{\pi}{N}\right) + \cos\left(\frac{2\pi}{N}\right) \right] \tan\left(\frac{\pi}{N}\right) + \mathcal{O}(\lambda). \end{aligned} \quad (33)$$

To decompose the Hopf normal form [Eq. (29)] into radial and phase dynamics, we transform to polar coordinates (r_{k^*}, φ_{k^*}) , such that $z_{k^*} = r_{k^*} e^{i\varphi_{k^*}}$, leading us to:

$$\tau_0 \dot{r}_{k^*} \sim \left(\mu_{k^*} - \mathcal{A}_{k^*} r_{k^*}^2 \right) r_{k^*}, \quad (34)$$

$$\tau_0 \dot{\varphi}_{k^*} \sim \omega_{k^*} - \mathcal{B}_{k^*} r_{k^*}^2. \quad (35)$$

The structure of radial dynamics (34) admits an additional attractor with $\dot{r}_{k^*} = 0$, $\dot{\varphi}_{k^*} \neq 0$ for some finite $r_{k^*}^* > 0$, in addition to $r_{k^*} = 0$, which corresponds to the trivial fixed point \mathbf{v}^* . This additional attractor corresponds to a limit cycle, characterizing the oscillations observed in Figs. 2 and 3. To analyze this limit cycle,

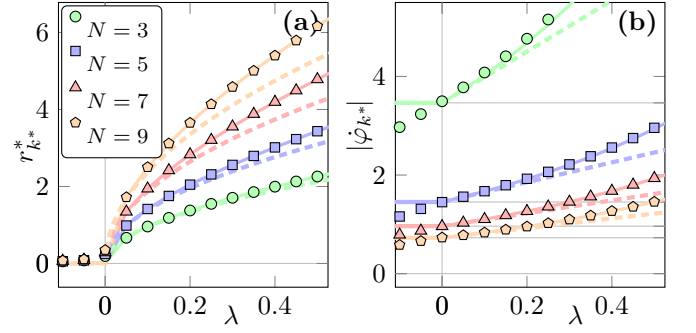


FIG. 4. Small-amplitude oscillations in the thermodynamic limit as function of λ and for different numbers of inverters N . (a) Amplitude $r_{k^*}^*$ from Eq. (36) (dashed lines), from numerical solution of Eqs. (11) (solid lines), and from Gillespie simulations [47] with $\Omega = 10^4$ (symbols). (b) Angular velocity $|\dot{\varphi}_{k^*}|$ from Eq. (37) (dashed lines), from numerical solution of Eqs. (11) (solid lines), and from Gillespie simulations with $\Omega = 10^4$ (symbols).

we first obtain for $\lambda > 0$ the positive fixed point $r_{k^*}^*$ of Eq. (34) as,

$$r_{k^*}^{*2} \sim \frac{\mu_{k^*}}{\mathcal{A}_{k^*}} \sim \frac{N^2}{2 \left[\cos^2\left(\frac{\pi}{2N}\right) - \frac{1}{4} \right]} \lambda. \quad (36)$$

Hence, we find that for $\lambda \ll 1$, the amplitude of the oscillations increases with the applied voltage and the number of inverters as $r_{k^*}^* \propto N\sqrt{\lambda} = N\sqrt{(V_{dd} - V_{dd}^*)/V_T}$.

Figure 4(a) shows $r_{k^*}^*$ as a function of λ close to the bifurcation as obtained from Eq. (36), compared with Gillespie simulations [47] of the stochastic voltage vector \mathbf{v} at large systems size and with numerical solutions of the deterministic dynamics (11). We observe good agreements between all methods for $\lambda \ll 1$.

Similarly, the angular velocity $\dot{\varphi}_{k^*}$ experiences corrections of order λ for $\lambda > 0$, as the system is driven away from the unstable fixed point. These angular velocity corrections can be computed from Eq. (35), we find

$$\tau_0 \dot{\varphi}_{k^*} \sim \omega_{k^*}|_{\lambda=0} \left[1 + \frac{\cos^2\left(\frac{\pi}{2N}\right)}{\cos^2\left(\frac{\pi}{2N}\right) - \frac{1}{4}} \lambda \right]. \quad (37)$$

The second term in the brackets is positive for all odd $N \geq 3$, suggesting that the frequency of oscillations increases with increasing λ , to leading order in λ . This finding is confirmed in Fig. 4(b), which shows $|\dot{\varphi}_{k^*}|$ from Gillespie simulations, from a numerical solution of Eq. (11), and from the theory in Eq. (37). The numerical results are in good agreement with the theory for small positive λ . For larger λ , the frequency-increasing effect of oscillations becomes even stronger due to higher-order corrections in λ , which are not captured by Eq. (37).

D. Stability

The stability of oscillating states is determined by a linear stability analysis of Eq. (34). The limit cycle

corresponding to $r_{k^*}^*$ is stable if the derivative $\mathbb{N}_{k^*} \equiv \partial \dot{r}_{k^*} / \partial r_{k^*} |_{r_{k^*}=r_{k^*}^*}$ of the amplitude flow (34) is negative when evaluated on the limit cycle, i.e.,

$$\mathbb{N}_{k^*} = (\mu_{k^*} - 3\mathcal{A}_{k^*} r_{k^*}^{*2}) = -2\mu_{k^*} < 0. \quad (38)$$

Equation (38) confirms that the limit cycle is stable with respect to transverse disturbances for $\lambda > 0$. Along the direction along the limit cycle, the stability exponent vanishes, $\partial \dot{\varphi}_{k^*} / \partial \varphi_{k^*} = 0$, which means that longitudinal disturbances neither grow nor shrink. This enables free diffusion along the limit cycle, leading to long-time decoherence of the phase φ_{k^*} , which we explore in Sec. IV C.

A simple measure for the overall local stability of a given state is the so-called phase-space contraction rate \mathcal{L} . It measures by how much infinitesimal phase-space volumes are contracted in the vicinity of a given state. We define the dimensionless phase-space contraction rate as [49]

$$\mathcal{L} = -\tau_0 \sum_{n=0}^{N-1} \frac{\partial \dot{v}_n}{\partial v_n}. \quad (39)$$

Using the dynamics (25) close to the bifurcation and the Fourier transform, we can write \mathcal{L} as

$$\mathcal{L} \sim \mathcal{L}_0 + \frac{8}{N} \cos^2\left(\frac{\pi}{2N}\right) r_{k^*}^{*2}, \quad (40)$$

where $\mathcal{L}_0 = 2N$ is the phase-space contraction rate at the fixed point. Equation (40) shows that the rate of phase-space contraction increases in the presence of small amplitude oscillations for $\lambda > 0$. We define the relative change $\Delta\mathcal{L}$ of the phase-space contraction rate as

$$\begin{aligned} \Delta\mathcal{L} &= \frac{\mathcal{L} - \mathcal{L}_0}{|\mathcal{L}_0|} \sim \frac{4}{N^2} \cos^2\left(\frac{\pi}{2N}\right) r_{k^*}^{*2}, \\ &\sim \frac{2 \cos^2\left(\frac{\pi}{2N}\right)}{\cos^2\left(\frac{\pi}{2N}\right) - \frac{1}{4}} \lambda > 0, \end{aligned} \quad (41)$$

for $\lambda > 0$. We will return to this relation in Sec. III E.

E. Entropy production rate

Small-amplitude oscillations for $\lambda > 0$ are facilitated by a constant non-equilibrium drive across each inverter. This drive keeps the system far from equilibrium and renders the dynamics irreversible. This irreversibility in turn is characterized by a finite rate of irreversible entropy production $\dot{\Sigma}$. In the large system-size limit ($\Omega \rightarrow \infty$), the time-averaged entropy production is equal to the time-averaged heat dissipated by the transistors [11, 18]. Since the currents through the transistors and thus the entropy production scale with the size of the system Ω , it is convenient to introduce the intensive entropy production rate $\dot{\sigma} \equiv \dot{\Sigma}/\Omega$.

Following the previous discussion, $\dot{\sigma}$ can be directly computed from the macroscopic transition rates $\omega_{i\pm}^{p/n}$ [50], averaged over a period T of the limit cycle:

$$\begin{aligned} \dot{\sigma} &= \frac{\tau_0}{T} \sum_{i=0}^{N-1} \sum_{\rho=n,p} \int_0^T dt [\omega_{i+}^\rho(\mathbf{v}) - \omega_{i-}^\rho(\mathbf{v})] \log \frac{\omega_{i+}^\rho(\mathbf{v})}{\omega_{i-}^\rho(\mathbf{v})}, \\ &= \left(\frac{2V_{dd}}{TV_T}\right) \sum_{n=0}^{N-1} \int_0^T dt [e^{V_{dd}/V_T} \cosh(v_{n-1}) - \cosh(v_n - v_{n-1})]. \end{aligned} \quad (42)$$

In this dimensionless formulation, the Ω -scaled entropy production rate $\dot{\sigma}$ is measured in units of k_B/τ_0 , where k_B denotes Boltzmann's constant. Close to the bifurcation, for $\lambda > 0$, $\lambda \ll 1$, we have

$$\begin{aligned} \dot{\sigma} &\sim \dot{\sigma}_0 + \left(\frac{2V_{dd}}{V_T N}\right) \left[e^{V_{dd}/V_T} - 4 \cos^2\left(\frac{\pi}{2N}\right) \right] r_{k^*}^{*2}, \\ &\sim \dot{\sigma}_0 \left\{ 1 + \left[\frac{1}{2} - \cos\left(\frac{\pi}{N}\right) \right] \frac{4}{N^2} \cos^2\left(\frac{\pi}{2N}\right) r_{k^*}^{*2} \right\}. \end{aligned} \quad (43)$$

where $\dot{\sigma}_0 = (2V_{dd}N/V_T) (e^{V_{dd}/V_T} - 1)$ denotes the entropy production rate at the fixed point \mathbf{v}^* . Note that the time average in Eq. (42) disappears close to the bifurcation [see Eq. (43)], because $r_{k^*}^*$ remains constant on the limit cycle to linear order in λ .

As $1/2 - \cos(\pi/N) < 0$ for $N > 3$, Eq. (43) shows that dissipation is reduced compared to $\dot{\sigma}_0$ by the presence of small-amplitude oscillations. For $N = 3$, one has $1/2 - \cos(\pi/3) = 0$, so entropy production does not change to linear order in λ close to the transition.

Figure 5(a) shows the entropy production rate $\dot{\sigma}$ as a function of λ obtained from (43) compared with our numerics for different N . We observe that $\dot{\sigma}$ generally increases with increasing λ . However, the difference $\dot{\sigma} - \dot{\sigma}_0$ is negative for $N > 3$, as predicted by Eq. (43). The case $N = 3$, by contrast, is somewhat special in that the linear contribution of small-amplitude oscillations in Eq. (43) vanishes. Furthermore, the numerical simulations in Fig. 5(a), show that the higher-order terms are *positive*, which means that dissipation *increases* due to oscillations when $N = 3$, in contrast to the opposite behavior for $N > 3$.

Defining the relative change $\Delta\dot{\sigma} = (\dot{\sigma} - \dot{\sigma}_0)/|\dot{\sigma}_0|$ of entropy production across the bifurcation, and using Eq. (41), we obtain the stability-dissipation relation

$$\Delta\dot{\sigma} \sim \left[\frac{1}{2} - \cos\left(\frac{\pi}{N}\right) \right] \Delta\mathcal{L}, \quad (44)$$

for $0 < \lambda \ll 1$. A similar relation has previously been derived for driven Potts models in Refs. [10, 11]. It shows that stability and dissipation are linearly related close to the bifurcation, and that decreasing dissipation corresponds to increasing local stability for $N > 3$. The linear relation (44) is confirmed by our numerics [51] in Fig. 5(b), which also shows that higher-order effects further away from the oscillation transition lead to a relative increase in $\Delta\dot{\sigma}$ compared to Eq. (44).

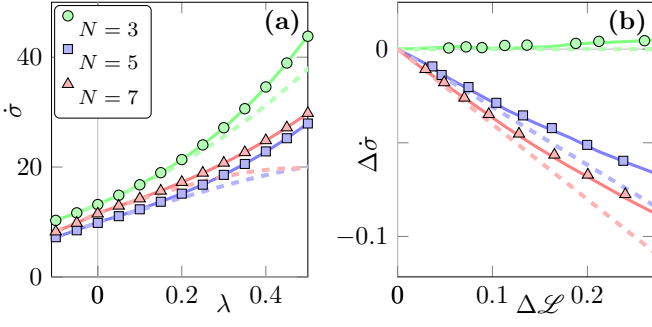


FIG. 5. (a) Entropy production rate $\dot{\sigma}$ as function of λ for different numbers N of inverters from Eq. (43) (dashed lines), from numerical solutions of Eq. (42), and from Gillespie simulations with $\Omega = 10^3$ (symbols). (b) Stability-dissipation relation (44) compared with the numerical solution of Eqs. (11) (solid lines) and Gillespie simulations (symbols).

To conclude this Section, we have characterized the small-amplitude oscillations close to the critical voltage V_{dd}^*/V_T for any odd number of inverters. We find that the dynamics of ring oscillators in the long-time limit ($t/\tau_0 \rightarrow \infty$) relaxes into a stable oscillating state, characterized by a limit cycle with an increased phase-space contraction rate. In terms of the voltages v_n , the small-amplitude oscillations are given by

$$v_n(t) = (-1)^n \frac{2V_T}{N} r_{k^*}^* \cos\left(\dot{\varphi}_{k^*} t - \frac{n\pi}{N}\right) + \mathcal{O}(\lambda), \quad (45)$$

where the amplitude $r_{k^*}^*$ and the frequency $\dot{\varphi}_{k^*}$ are obtained in Eqs. (36) and (37), respectively. For $N > 3$, the presence of oscillations decreases dissipation but increases stability, as summarized by a stability-dissipation relation (44).

IV. DEVIATIONS FROM THERMODYNAMIC LIMIT

In our analysis of the thermodynamic limit in Sec. III we have neglected finite-size voltage fluctuations. Such fluctuations are, however, present in any finite system, and are expected to be particularly relevant close to the oscillation transition. Going beyond the thermodynamic limit, we consider large but finite systems under the influence of weak finite-size fluctuations.

To this end, we perturbatively expand the Master equation (7) to next-to-leading order in the system size Ω to capture the leading fluctuations. Although not generally suited to characterize global properties, such as fluctuation theorems, which depend on fluctuations of all magnitudes [45], such an expansion faithfully describes Gaussian fluctuations around the deterministic limit cycle discussed in Sec. III C.

Expanding (7) up to $\mathcal{O}(1/\Omega)$, we obtain the Fokker-

Planck equation

$$\partial_t P(\mathbf{v}, t) \sim -\nabla_{\mathbf{v}} \cdot [\mathbf{F}(\mathbf{v}) P(\mathbf{v}, t)] + \frac{1}{\Omega} \nabla_{\mathbf{v}}^T [\hat{\mathbb{D}}(\mathbf{v}) \nabla_{\mathbf{v}} P(\mathbf{v}, t)], \quad (46)$$

with diffusion matrix \hat{D}_{ij} given by

$$\hat{D}_{ij} = \frac{1}{\tau_0} \left[\cosh\left(\frac{v_i - v_{i-1}}{V_T}\right) + e^{V_{\text{dd}}/V_T} \cosh\left(\frac{v_{i-1}}{V_T}\right) \right] \delta_{ij}, \quad (47)$$

which is in diagonal form for the given model. Equation (46) corresponds to the following stochastic differential equation for the voltage vector \mathbf{v} :

$$\frac{dv_i}{V_T} = F_i(\mathbf{v}) dt + \sqrt{\frac{2\hat{D}_{ii}(\mathbf{v})}{\Omega}} \circ dW_i. \quad (48)$$

Here, $\circ dW_i$ are independent Wiener increments in the Stratonovich convention [52], with $\langle dW_i^2(t) \rangle = dt$.

A. Stochastic normal form

To analyze Eq. (48) further, we bring it into the stochastic version of the normal form (29), sometimes called “stochastic normal form” [43], which captures the fluctuations to leading order, close to the deterministic normal-form behavior.

In the weak-noise limit close to the bifurcation, there are two small parameters: The distance λ from the bifurcation and the inverse system size Ω^{-1} , which fixes the noise strength. To identify the leading noise-induced effects close to the bifurcation, we expand \hat{D}_{ij} to the lowest order in λ , so that $D_{ii}(\mathbf{v}) \sim (1 + e^{V_{\text{dd}}^*/V_T})/\tau_0$. Taking the discrete Fourier transform of Eq. (48) and using the normal form in Sec. III C for \mathbf{F} , we obtain the stochastic equation

$$dz_{k^*} \sim \tau_0^{-1} \left(\mathcal{D}_{k^*} - \mathcal{C}_{k^*} |z_{k^*}|^2 \right) z_{k^*} dt + \sqrt{\frac{2\bar{D}}{\Omega}} \circ d\hat{W}_{k^*}, \quad (49)$$

where $\bar{D} = N(1 + e^{V_{\text{dd}}^*/V_T})/(2\tau_0)$. Furthermore,

$$d\hat{W}_{k^*} = \sqrt{\frac{2}{N}} \sum_{n=0}^{N-1} e^{i2\pi n k^*} \circ dW_n, \quad (50)$$

is the weighted sum of N independent Wiener increments, which is itself a complex Wiener increment, $d\hat{W}_{k^*} = d\hat{W}_{k^*}^{\Re} + i d\hat{W}_{k^*}^{\Im}$, with $\langle d\hat{W}_{k^*}^{\Re}(t)^2 \rangle = \langle d\hat{W}_{k^*}^{\Im}(t)^2 \rangle = dt$ and $\langle d\hat{W}_{k^*}^{\Re}(t) d\hat{W}_{k^*}^{\Im}(t) \rangle = 0$.

We again transform into polar coordinates (r_{k^*}, φ_{k^*}) to obtain the stochastic phase-amplitude equations in the presence of finite-size fluctuations. For computational convenience, we first transform the coordinates and then move from the Stratonovich to the Itô convention [52] to simplify the manipulations that follow.

In this way, we obtain stochastic phase-amplitude equations, given by

$$dr_{k^*} \sim \tau_0^{-1} \left(\mu_{k^*} r_{k^*} - \mathcal{A}_{k^*} r_{k^*}^3 + \frac{\tau_0 \bar{D}}{r_{k^*} \Omega} \right) dt + \sqrt{\frac{2\bar{D}}{\Omega}} \cdot d\hat{W}_t^r, \quad (51a)$$

$$d\varphi_{k^*} \sim \tau_0^{-1} (\omega_{k^*} - \mathcal{B}_{k^*} r_{k^*}^2) dt + \frac{1}{r_{k^*}} \sqrt{\frac{2\bar{D}}{\Omega}} \cdot d\hat{W}_t^\varphi, \quad (51b)$$

where $d\hat{W}_t^r$ and $d\hat{W}_t^\varphi$ are independent Wiener increments in Itô convention with $\langle d\hat{W}_t^r \rangle = \langle d\hat{W}_t^\varphi \rangle = dt$ and $\langle d\hat{W}_t^r d\hat{W}_t^\varphi \rangle = 0$, which characterize finite-size fluctuations.

The presence of finite-size noise in the phase-amplitude equations has important consequences that we discuss in the following.

B. Noise-induced oscillations

In the presence of finite-size voltage fluctuations, the system oscillates even for $\lambda \leq 0$, i.e., below and at the bifurcation. Such noise-induced oscillations arise as a combination of finite-size noise and the system's oscillatory relaxation towards its fixed point. More precisely, for $\lambda \leq 0$, finite-size voltage fluctuations drive the system away from the stable fixed point, by means of the noise-induced term $\bar{D}/(r_{k^*}\Omega)$ in Eq. (51a). This term, together with the noise term in Eq. (51a), vanishes as $\Omega \rightarrow \infty$, resulting in the deterministic dynamics discussed in Sec. III.

As a consequence of this, oscillations are no longer characterized by a single closed limit cycle as in Sec. III but by a probability density of possible amplitudes r_{k^*} and phases φ_{k^*} . To quantify the amplitudes of noise-induced fluctuations in the long-time limit, we first compute the steady-state probability density $P_s(r_{k^*})$ from the Fokker-Planck equation corresponding to Eq. (51a). This leads us to

$$P_s(r_{k^*}) = \mathcal{N}^{-1} r_{k^*} \exp \left[-\frac{1}{\zeta} \left(\frac{\mathcal{A}_{k^*}}{\mu_{k^*}} r_{k^*}^2 - 1 \right)^2 \right], \quad (52)$$

where the normalization \mathcal{N} is given by

$$\mathcal{N} = \frac{\sqrt{\pi}}{4} \frac{\zeta |\mu_{k^*}|}{\mathcal{A}_{k^*}} \left[\operatorname{erf} \left(\frac{1}{\zeta} \right) + 1 \right]. \quad (53)$$

In Eq. (52), we have defined the dimensionless parameter

$$\zeta \equiv \sqrt{\frac{4\mathcal{A}_{k^*}\bar{D}\tau_0}{\Omega\mu_{k^*}^2}}, \quad (54)$$

which quantifies the importance of finite-size fluctuations. Sufficiently far away from the bifurcation for $\mu_{k^*} \propto \lambda \gg \Omega^{-1/2}$, fluctuations are mostly irrelevant, and we have $\zeta \ll 1$. In this case, Eq. (52) strongly focusses

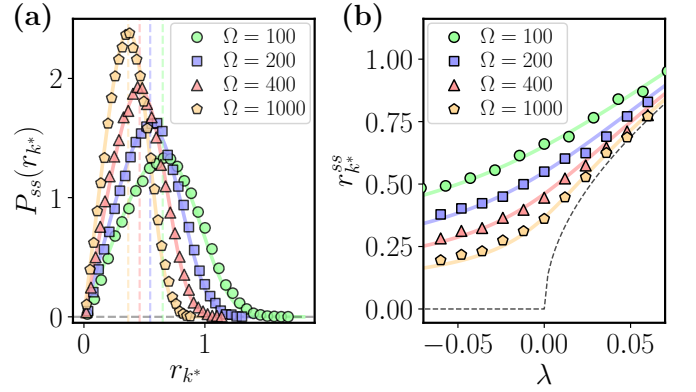


FIG. 6. Finite-size fluctuations close to the bifurcation for $N = 3$ and different Ω . (a) Steady-state probability density $P_s(r_{k^*})$ at $\lambda = 0$ obtained from Eq. (52) (lines) and from Gillespie simulations (symbols). (b) Most likely radius $r_{k^*}^{ss}$ in the steady state as a function of λ from Eq. (55) (lines) and Gillespie simulations (symbols). The dashed black line corresponds to the thermodynamic limit ($\Omega \rightarrow \infty$) from Eq. (36).

around the maximum of the distribution. Close to the bifurcation $\lambda \ll \Omega^{-1/2}$, by contrast, we have $\zeta \gg 1$. In this case, finite-size fluctuations are important even as the system size tends to infinity.

In particular, the significance of ζ is understood by comparing the most likely amplitude $r_{k^*}^{ss}$ with the magnitude of fluctuations around $r_{k^*}^{ss}$. The most likely amplitude $r_{k^*}^{ss}$ is obtained from Eq. (52), by solving $P'_s(r_{k^*}^{ss}) = 0$ for $r_{k^*}^{ss}$, which gives

$$r_{k^*}^{ss2} = \frac{|\mu_{k^*}|}{2\mathcal{A}_{k^*}} \left[\operatorname{sign}(\lambda) + \sqrt{1 + \zeta^2} \right]. \quad (55)$$

In the deterministic limit $\zeta \rightarrow 0$, Eq. (55) reduces to $r_{k^*}^{ss2} = 0$ for $\lambda < 0$ and $r_{k^*}^{ss2} = \mu_{k^*}/\mathcal{A}_{k^*}$ for $\lambda > 0$, in agreement with Eq. (36). For $\zeta \gg 1$, i.e., close to the bifurcation, we find $r_{k^*}^{ss2} \sim \sqrt{\bar{D}\tau_0/(\Omega\mathcal{A}_{k^*})} > 0$. Hence, as advertised earlier, finite-size fluctuations may induce coherent oscillations of finite amplitude, close to and even at the bifurcation, which are absent in the deterministic dynamics in Sec. III.

The magnitude of Gaussian fluctuations $\sigma_{k^*}^{ss}$ around $r_{k^*}^{ss}$ is estimated from $\sigma_{k^*}^{ss2} \sim P''_s(r_{k^*}^{ss})$, which gives

$$\sigma_{k^*}^{ss2} \sim \frac{|\mu_{k^*}|}{2\mathcal{A}_{k^*}} \frac{\zeta^2}{4(1 + \zeta^2)^{1/2}}. \quad (56)$$

This expression shows that in the deterministic limit $\zeta \rightarrow 0$, fluctuations around $r_{k^*}^{ss}$ (of order $\sigma_{k^*}^{ss}$), decay as $\zeta \propto \Omega^{-1/2}$. Close to the bifurcation, for $\zeta \gg 1$, we have $\sigma_{k^*}^{ss2} \sim \sqrt{\bar{D}\tau_0/(\Omega\mathcal{A}_{k^*})}/4$ which is of the same order as $r_{k^*}^{ss2}$. This implies that when ζ is large, fluctuations play a significant role, regardless of the system size, which is a common property of fluctuations close to a phase transition [53].

Figure 6(a) shows $P_s(r_{k^*})$ obtained using Eq. (52) and from Gillespie simulations at the bifurcation $\lambda = 0$

($\zeta \rightarrow \infty$), for $N = 3$ and for different system sizes Ω . We observe that Eq. (52) vanishes for small and large values of r_{k^*} and exhibits a maximum around its most probable value, which decreases as the thermodynamic limit $\Omega \rightarrow \infty$ is approached. In all cases, Eq. (52) accurately captures the steady-state density. Along with the maximum value, the magnitudes of fluctuations around $r_{k^*}^{ss}$ decrease. As we have shown in Eqs. (55) and (56), the ratio between $r_{k^*}^{ss}$ and $\sigma_{k^*}^{ss}$ converges to a fixed value of order unity, $\sigma_{k^*}^{ss}/r_{k^*}^{ss} \rightarrow 2$ as $\Omega \rightarrow \infty$, indicating that fluctuations remain important close to the bifurcation at arbitrary system size.

Figure 6(b) shows $r_{k^*}^{ss}$ as a function of λ for $N = 3$ and varying system size, from simulations and Eq. (55). In good agreement between theory and simulations, we observe that $r_{k^*}^{ss}$ approaches the deterministic amplitude $r_{k^*}^*$ (36) as Ω increases at fixed λ , i.e., ζ decreases. Finally note that, for increasing Ω , the region around the bifurcation where fluctuations are relevant, i.e., ζ is not small, shrinks as $\Omega^{-1/2}$.

C. Phase decoherence

As mentioned in the context of the stability analysis in Sec. IIID, finite-size fluctuations of the phase φ can propagate unobstructed in the longitudinal direction along the limit cycle. This causes φ_{k^*} to diffuse freely along the limit cycle, leading to a long-term decoherence of the phase. This phase decoherence is harnessed when ring oscillators are used as true random-number generators [31–33], because the phase difference between several ring oscillators is sensitive to “truly random” finite-size fluctuations. In this context, the rate at which independent, true random numbers can be generated is related to the decoherence time of φ_{k^*} . We now estimate this decoherence time from the stochastic normal form (51).

The decoherence time τ_c of stochastic oscillations is quantified by the inverse exponential rate at which the auto-correlation function $\mathcal{C}_n(\tau) = \langle v_n(t)v_n(t+\tau) \rangle$ decays as a function of τ for $\tau, t \gg \tau_0$. In other words, the decoherence time τ_c estimates the time over which an ensemble of initially coherent oscillators loses its coherence due to phase noise, eventually leading to uniform randomness of the output v_n .

At large but finite system size $\Omega \gg 1$, we obtain an expression for τ_c by expanding the radial dynamics around the most probable value $r_{k^*}^{ss}$ of the stationary distribution. In Appendix A, we show that such an expansion can be consistently formulated as long as the parameter

$$\bar{\varepsilon} \equiv f_{\text{sign}(\lambda)}(\zeta), \quad (57)$$

becomes small for large system size, i.e., $\bar{\varepsilon} \ll 1$ for $\Omega \gg 1$. The function f_{\pm} has the form

$$f_{\pm}(\zeta) = \frac{\zeta}{2} \left(\sqrt{1+\zeta^2} \pm 2 \right) \left(\sqrt{1+\zeta^2} \pm 1 \right)^{-\frac{1}{2}} (1+\zeta^2)^{-\frac{3}{4}}. \quad (58)$$

From an analysis of $f_{\pm}(\zeta)$ we find that $\bar{\varepsilon}$ becomes small sufficiently far away from the bifurcation for $\zeta \ll 1$. In this case, one has

$$\bar{\varepsilon} = f_{+}(\zeta) \sim \frac{3\zeta}{\sqrt{8}} \ll 1. \quad (59)$$

This finding is intuitive because $\zeta \ll 1$ corresponds to the case when fluctuations are small, as discussed in Sec. IV B.

In the opposite limit, for $\zeta \gg 1$, i.e., close to the bifurcation, $\bar{\varepsilon}$ remains of order unity even as $\Omega \rightarrow \infty$. The same holds outside the oscillating phase, for $\lambda < 0$. In these regimes, expanding the dynamics around the maximum $r_{k^*}^{ss}$ is uncontrolled.

If $\bar{\varepsilon} \ll 1$, on the other hand, the dynamics can be systematically expanded around $r_{k^*}^{ss}$. Based on such an expansion, we show in Appendix A that, to leading order, the decoherence time τ_c takes the form

$$\tau_c^{-1} \sim \frac{\bar{D}}{\Omega} \left(r_{k^*}^{ss-2} + \frac{\mathcal{B}_{k^*}^2 r_{k^*}^{ss2}}{\mathcal{A}_{k^*} r_{k^*}^{ss2} - \frac{\mu_{k^*}}{2}} \right). \quad (60)$$

In the deterministic limit $\zeta \ll 1$, this expression agrees with that found in [44], where the expansion was carried out around the deterministic radius $r_{k^*}^*$ in Eq. (36), instead of $r_{k^*}^{ss}$. The first term in Eq. (60) corresponds to decoherence due to phase diffusion with diffusion constant $D_{\varphi}(r_{k^*}^{ss}) = \bar{D}/(\Omega r_{k^*}^{ss2})$ evaluated at the maximum $r_{k^*}^{ss}$ of the radial distribution. The second term is a consequence of weak interactions between the radial and phase dynamics [44].

In the oscillating state sufficiently far away from the bifurcation, when $\bar{\varepsilon} \sim \zeta \ll 1$, we have $r_{k^*}^{ss} \sim \lambda^{1/2}$, so that Eq. (60) predicts τ_c to grow linearly with system size, i.e. $\tau_c \sim \Omega$ [42].

Close to the bifurcation for $\zeta \gg 1$, Eq. (60) is not strictly valid, as it is based on an uncontrolled approximation. However, since the range of validity of Eq. (60) approaches the bifurcation at $\lambda = 0$ as $\Omega \rightarrow \infty$, we speculate that Eq. (60) still predicts the dominant scaling of τ_c with Ω , albeit possibly with wrong prefactor, in the limit of infinite system size. In the regime $\zeta \gg 1$, $r_{k^*}^{ss}$ scales as $r_{k^*}^{ss} \sim \Omega^{-1/4}$, so that Eq. (60) predicts τ_c to increase as $\tau_c \sim \Omega^{1/2}$, substantially slower than away from the bifurcation. We confirm these scalings numerically below. Furthermore, these results are consistent with the findings in Ref. [15], where the authors numerically observed the same scalings close to and far away from bifurcations in several biochemical oscillator models.

Figure 7(a) shows τ_c at finite but large system size Ω as function of λ from Eq. (60) and from stochastic simulations with different numbers of inverters N . We observe good agreement between simulations and theory sufficiently far away from the bifurcation, i.e., to the right of the dashed line where $\zeta \lesssim 1$. The decoherence time τ_c increases with the number N of inverters for fixed λ , due to the increase of the most-likely amplitude $r_{k^*}^{ss}$ in Eq. (60).

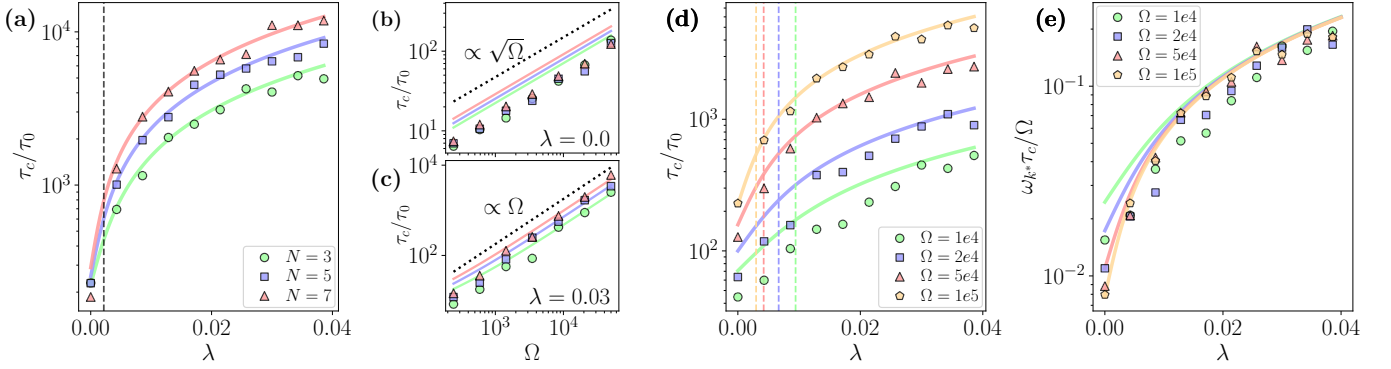


FIG. 7. Decoherence time τ_c as a function of different parameters. Symbols denote adaptive tau-leaping simulations [54]. The solid lines are derived from Eq. (60) and Eq. (37). The dashed vertical lines show where $\zeta \approx 1$ for given N and Ω . (a) τ_c as a function of λ for different number of inverters N at system size $\Omega = 10^5$. (b) τ_c as a function of the system size Ω at fixed $\lambda = 0$, and (c) at fixed $\lambda = 0.03$, for the same values of N . (d) τ_c as a function of λ for different system sizes Ω with $N = 3$ inverters. (e) Scaled quality factor $\omega_k^* \tau_c / \Omega$ as function of λ for different system sizes Ω with $N = 3$ inverters.

Figure 7(b) shows the scaling of τ_c as a function of Ω for $\zeta \gg 1$. The numerical data confirm our previous expectation that Eq. (60) should correctly predict the $\sim \Omega^{1/2}$ scaling close to the bifurcation, although the expansion around $r_{k^*}^{ss}$ is not controlled [$\bar{\varepsilon}$ in Eq. (57) is not small]. However, the prefactor appears to be incorrect. Figure 7(c) shows the scaling away from the bifurcation, where ζ becomes small for the largest system sizes. In this case, both the $\sim \Omega$ scaling and the prefactor are correctly predicted by Eq. (60).

This behavior is summarized for $N = 3$ in Fig. 7(d), which shows τ_c as a function of λ for a range of different system sizes. The vertical dashed lines show where $\zeta = 1$. The figure shows how Eq. (60) becomes increasingly accurate with increasing system size, even close to $\lambda = 0$.

Finally, we briefly comment on the relevance of the scaling properties of τ_c for the Ω -scaled quality factor $\omega_k^* \tau_c / \Omega$ [15, 44, 55, 56], which is a measure for the number of coherent oscillations (scaled by Ω) that the system is able to perform before losing its coherence. The Ω -scaled quality factor has been shown to be bounded from above for thermodynamically consistent models by a constant of order unity [44, 55, 56]. Since ω_k^* becomes independent of Ω for large system size, see Eq. (37), the Ω -scaling of the quality factor $\omega_k^* \tau_c$ corresponds to the scaling of τ_c . That is, after scaling with Ω , $\omega_k^* \tau_c / \Omega$ tends to a constant for $\zeta \ll 1$, away from the bifurcation. Close to the bifurcation for $\zeta \gg 1$, by contrast, it approaches zero as $\Omega^{-1/2}$ for a large system size.

This behavior is shown in Fig. 7(e), which depicts $\omega_k^* \tau_c / \Omega$ as a function of λ for different system sizes from theory and numerics. We observe that while the scaled quality factor becomes independent of the system size far from the bifurcation, it decreases with increasing system size in the vicinity of $\lambda = 0$. In the entire λ range that we considered, the quality factor is significantly smaller than unity, so thermodynamic bounds such as those derived in Refs. [44, 55, 56] are irrelevant here. This statement is true in particular close to the bifurcation, where oscil-

lations are exceptionally decoherent, leading to a scaled quality factor that shrinks as $\Omega^{-1/2}$.

V. CONCLUSIONS

We analyzed small-amplitude oscillations and their fluctuations in N -stage CMOS ring oscillators operating in the subthreshold regime. Starting with a thermodynamically consistent model, we demonstrated that, in the thermodynamic limit $\Omega \rightarrow \infty$, oscillations emerge through a Hopf bifurcation resulting in a stable limit cycle when the supply voltage V_{dd} exceeds a critical threshold V_{dd}^* . Exploiting the symmetries of the model, we used a normal-form analysis to obtain explicit expressions for the limit cycle and its frequency for any odd N , which are valid close to the bifurcation. Employing the framework of stochastic thermodynamics, we showed that the entropy production $\dot{\sigma}$ of ring oscillators decreases in the presence of oscillations for $N > 3$, but increases sub-linearly for $N = 3$. The change $\Delta \dot{\sigma}$ in the entropy production across the bifurcation is linearly related to the change in phase-space contraction $\Delta \mathcal{L}$ through a stability-dissipation relation [Eq. (44)], similar to that found in Refs. [10, 11].

For large but finite devices $\Omega = V_T / v_e \gg 1$, we characterized finite-size fluctuations using a systematic system-size expansion to capture the lowest-order effects of fluctuations around the deterministic limit cycle. Using a stochastic version of the Hopf normal form, we showed that finite-size fluctuations remain relevant close to the bifurcation, even in the thermodynamic limit, which is a common feature in the vicinity of phase transitions. In this regime, we showed that fluctuations induce finite-amplitude oscillations, even at and below the critical voltage. These noise-induced oscillations are characterized by an anomalously short decoherence time that was shown to scale sub-linearly $\tau_c \sim \Omega^{1/2}$ with Ω .

This exceptional fast decoherence offers a route to-

ward tunable randomness in probabilistic hardware, such as deterministic “Ising machines” [57–59] or stochastic probabilistic-bit systems [60]. Assessing the practical feasibility of such approaches and benchmarking them against existing subthreshold-CMOS p-bit implementations [26], remains an important direction for future work.

A key limitation of our analysis is that supply voltages must be small, of the order of the thermal voltage ($\sim 26\text{ mV}$ at room temperature). Further investigations are required to determine whether the permutation symmetry used here allows for simplifications, even further away from the critical voltage.

ACKNOWLEDGMENTS

This research was supported by the Project No. INTER/FNRS/20/15074473 funded by F.R.S.-FNRS (Belgium) and FNR (Luxembourg).

Appendix A: Decoherence timescale calculation - Stochastic Normal Form

We present the details for the computation of the decorrelation time for the stochastic normal form (51). We again consider

$$dr_{k^*} \sim -\tau_0^{-1} V'(r_{k^*}) dt + \sqrt{\frac{2\bar{D}}{\Omega}} \cdot d\hat{W}_t^r, \quad (\text{A1a})$$

$$d\varphi_{k^*} \sim \tau_0^{-1} (\omega_{k^*} - \mathcal{B}_{k^*} r_{k^*}^2) dt + \frac{1}{r} \sqrt{\frac{2\bar{D}}{\Omega}} \cdot d\hat{W}_t^\varphi, \quad (\text{A1b})$$

where

$$V(r) = -\frac{\mu_{k^*} r^2}{2} + \mathcal{A}_{k^*} \frac{r^4}{4} - \frac{\bar{D}\tau_0}{\Omega} \log(r). \quad (\text{A2})$$

We proceed by expanding $V(r)$ around its minimum at $r_{k^*}^{ss}$, see Eq. (55). This yields for $V'(r_{k^*})$,

$$V'(r_{k^*}) \sim V'(r^*) + V''(r_{k^*}^{ss})(r_{k^*} - r_{k^*}^{ss}) + \frac{1}{2} V'''(r^*)(r_{k^*} - r_{k^*}^{ss})^2. \quad (\text{A3})$$

The minimum condition requires $V'(r_{k^*}^{ss}) = 0$, and we have

$$\kappa \equiv V''(r_{k^*}^{ss}) = 2|\mu_{k^*}| \sqrt{1 + \zeta^2}, \quad (\text{A4})$$

$$\xi \equiv V'''(r_{k^*}^{ss}) = 6\mathcal{A}_{k^*} r_{k^*}^{ss} - \frac{2\bar{D}\tau_0}{r_{k^*}^{ss3}\Omega}, \quad (\text{A5})$$

We thus obtain the following expression for the dynamics of $\rho = r_{k^*} - r_{k^*}^{ss}$:

$$d\rho \sim -\tau_0^{-1} (\kappa\rho + \xi\rho^2) dt + \sqrt{\frac{2\bar{D}\tau_0}{\Omega}} \cdot d\hat{W}_t^r. \quad (\text{A6})$$

We rescale ρ according to $\rho = \sqrt{\bar{D}\tau_0/(\Omega\kappa)} \bar{\rho}$ and time as $t = \tau_0 \bar{t}/\kappa$. This way, Eq. (A6) depends on a single parameter. We obtain

$$d\bar{\rho} \sim (-\bar{\rho} - \bar{\varepsilon}\bar{\rho}^2) d\bar{t} + \sqrt{2} \cdot d\hat{W}_{\bar{t}}^r, \quad (\text{A7})$$

with the parameter

$$\bar{\varepsilon} \equiv \sqrt{\frac{\bar{D}\tau_0}{\Omega\kappa^3}} \xi, \quad (\text{A8})$$

which agrees with Eq. (57) when expressed in terms of ζ . For small $\bar{\varepsilon}$, we expand

$$\bar{\rho} \sim \bar{\rho}^{(0)} + \bar{\varepsilon}\bar{\rho}^{(1)} + \bar{\varepsilon}^2\bar{\rho}^{(2)} + \dots, \quad (\text{A9})$$

and evaluate the resulting equation (A7) order by order in $\bar{\varepsilon}$. To linear order in $\bar{\varepsilon}$, we find

$$d\bar{\rho}^{(0)} \sim -\bar{\rho}^{(0)} d\bar{t} + \sqrt{2} \cdot d\hat{W}_{\bar{t}}^r, \quad (\text{A10})$$

$$d\bar{\rho}^{(1)} \sim -(1 + 2\bar{\rho}^{(0)})\bar{\rho}^{(1)} d\bar{t}. \quad (\text{A11})$$

To lowest order in $\bar{\varepsilon}$, $\bar{\rho}^{(0)}$ is a standard Ornstein-Uhlenbeck process, while $\bar{\rho}^{(1)}$ is a non-Gaussian correction, that we disregard in the following. We note, however, that systematic expansions around the lowest order process $\bar{\rho}^{(0)}$ can be constructed in this way.

We now consider the correlation function in the long-time limit

$$C_n(\tau) = \langle \nu_n(\tau) \nu_n(0) \rangle \sim \left(\frac{V_T}{N} \right)^2 \mathcal{C}(\tau) + \text{c.c.}, \quad (\text{A12})$$

where $\mathcal{C}(\tau) = \langle z_{k^*}(\tau) \bar{z}_{k^*}(0) \rangle$ and c.c. denotes the complex conjugate. To study the exponential decay of $C_n(\tau)$ we thus evaluate

$$\mathcal{C}(\tau) = \langle r_{k^*}(\tau) r_{k^*}(0) e^{i[\varphi_{k^*}(\tau) - \varphi_{k^*}(0)]} \rangle. \quad (\text{A13})$$

Integrating (A1b), we obtain

$$\begin{aligned} \varphi_{k^*}(\tau) - \varphi_{k^*}(0) &= \kappa^{-1} \int_0^{\tau\kappa} f[r_{k^*}(\bar{t})] d\bar{t} \\ &+ \sqrt{\frac{2\bar{\varepsilon}^2\kappa^2}{\xi^2}} \int_0^{\tau\kappa} g[r_{k^*}(\bar{t})] \cdot d\hat{W}_{\bar{t}}^\varphi, \end{aligned} \quad (\text{A14})$$

where $f(r_{k^*}) = \omega_{k^*} - \mathcal{B}_{k^*} r_{k^*}^2$ and $g(r_{k^*}) = 1/r_{k^*}$. In order to evaluate $\mathcal{C}(\tau)$, we first average over $\hat{W}_{\bar{t}}^\varphi$, conditional on a fixed $\{r_{k^*}(\bar{t})\}_{\bar{t} \in [0, \tau]}$, leading to

$$\mathcal{C}(\tau) = \left\langle r_{k^*}(\tau) r_{k^*}(0) \left\langle e^{i(\varphi_\tau - \varphi_0)} \left| \{r_{k^*}(t)\} \right\rangle_{\{\tilde{W}_t^\varphi\}} \right\rangle_{\{r_{k^*}(t)\}} = \left\langle r_{k^*}(\tau) r_{k^*}(0) e^{i\kappa^{-1} \int_0^{\tau\kappa} f[r_{k^*}(\bar{t})] d\bar{t} - \frac{\bar{\epsilon}^2 \kappa^2}{\xi^2} \int_0^{\tau\kappa} g^2[r_{k^*}(\bar{t})] d\bar{t}} \right\rangle_{\{r_{k^*}(t)\}}. \quad (\text{A15})$$

We express $r_{k^*}(\bar{t})$ as $r_{k^*}(\bar{t}) = r_{k^*}^{ss} + \bar{\epsilon}(\kappa/\xi)\bar{\rho}(\bar{t})$ and use the small- $\bar{\epsilon}$ expansion (A9) to find to lowest non-vanishing order in $\bar{\epsilon}$

$$\mathcal{C}(\tau) \sim r_{k^*}^{ss2} e^{[i\omega_{k^*}^{ss} - \frac{\bar{\epsilon}^2 \kappa^3}{\xi^2} g^2(r_{k^*}^{ss})] \tau} \left\langle e^{i\frac{\bar{\epsilon}}{\xi} f'(r_{k^*}^{ss}) \int_0^{\tau\kappa} \bar{\rho}^{(0)}(\bar{t}) d\bar{t}} \right\rangle_{\{\rho(\bar{t})\}}, \quad (\text{A16})$$

$$\sim r_{k^*}^{ss2} e^{[i\omega_{k^*}^{ss} - \frac{\bar{\epsilon}^2 \kappa^3}{\xi^2} g^2(r_{k^*}^{ss})] \tau - \frac{\bar{\epsilon}^2}{2\xi^2} f'(r_{k^*}^{ss})^2 \text{Var}(\int_0^{\tau\kappa} \bar{\rho}^{(0)}(\bar{t}) d\bar{t})}, \quad (\text{A17})$$

where $\omega_{k^*}^{ss} = f(r_{k^*}^{ss}) = \omega_{k^*} - \mathcal{B}_{k^*} r_{k^*}^{ss2}$ corresponds to the oscillation frequency at $r_{k^*}^{ss}$. Evaluating $\text{Var}(\int_0^{\tau\kappa} \bar{\rho}^{(0)}(\bar{t}) d\bar{t})$

for long times $\tau\kappa \gg 1$ gives

$$\text{Var}\left(\int_0^{\tau\kappa} \bar{\rho}^{(0)}(\bar{t}) d\bar{t}\right) \sim 2\tau\kappa. \quad (\text{A18})$$

We thus obtain

$$\mathcal{C}(\tau) \sim r_{k^*}^{ss2} e^{i\omega_{k^*}^{ss} \tau - \tau/\tau_c}, \quad (\text{A19})$$

where we have identified the decorrelation time τ_c as

$$\tau_c^{-1} \sim \frac{\bar{\epsilon}^2 \kappa}{\tau_0 \xi^2} \left[\kappa^2 g^2(r_{k^*}^{ss}) + f'(r_{k^*}^{ss})^2 \right], \quad (\text{A20})$$

to leading order in $\bar{\epsilon}$. Reinstalling the original parameters and substituting the expressions for f and g we thus obtain

$$\tau_c^{-1} \sim \frac{\bar{D}}{\Omega \kappa^2} \left[\frac{\kappa^2}{r_{k^*}^{ss2}} + 4\mathcal{B}_{k^*}^2 r_{k^*}^{ss2} \right], \quad (\text{A21})$$

which agrees with Eq. (60) in the main text.

-
- [1] A. Goldbeter, *Biochemical Oscillations and Cellular Rhythms: The Molecular Bases of Periodic and Chaotic Behaviour* (Cambridge University Press, 1996).
 - [2] B. Novák and J. J. Tyson, Design principles of biochemical oscillators, *Nature Reviews Molecular Cell Biology* **9**, 981 (2008).
 - [3] S. H. Strogatz, *Nonlinear dynamics and chaos: with applications to physics, biology, chemistry, and engineering* (Chapman and Hall/CRC, 2024).
 - [4] G. Milburn, The thermodynamics of clocks, *Contemporary Physics* **61**, 69 (2020).
 - [5] G. P. Agrawal, Nonlinear fiber optics, in *Nonlinear Science at the Dawn of the 21st Century* (Springer, 2000) pp. 195–211.
 - [6] E. Buks and I. Martin, Self-excited oscillation and synchronization of an on-fiber optomechanical cavity, *Physical Review E* **100**, 032202 (2019).
 - [7] D. Rockwell and E. Naudascher, Self-sustaining oscillations of flow past cavities, *Journal of Fluids Engineering* **100**, 152 (1978).
 - [8] M. Golubitsky, I. Stewart, and D. Schaeffer, Singularities and groups in bifurcation theory II, *Applied Mathematical Sciences* **69** (1988).
 - [9] G. Nicolis, *Introduction to nonlinear science* (Cambridge University Press, 1995).
 - [10] J. Meibohm and M. Esposito, Minimum-dissipation principle for synchronized stochastic oscillators far from equilibrium, *Physical Review E* **110**, L042102 (2024).
 - [11] J. Meibohm and M. Esposito, Small-amplitude synchronization in driven potts models, *Physical Review E* **110**, 044114 (2024).
 - [12] P. C. Hohenberg and B. I. Halperin, Theory of dynamic critical phenomena, *Reviews of Modern Physics* **49**, 435 (1977).
 - [13] I. R. Epstein and K. Showalter, Nonlinear chemical dynamics: oscillations, patterns, and chaos, *The Journal of Physical Chemistry* **100**, 13132 (1996).
 - [14] T. Herpich, J. Thingna, and M. Esposito, Collective power: minimal model for thermodynamics of nonequilibrium phase transitions, *Physical Review X* **8**, 031056 (2018).
 - [15] B. Nguyen, U. Seifert, and A. C. Barato, Phase transition in thermodynamically consistent biochemical oscillators, *The Journal of Chemical Physics* **149** (2018).
 - [16] A. Gopal, N. Freitas, and M. Esposito, Information thermodynamics for Markov jump processes coupled to underdamped diffusion: Application to nanoelectromechanics, *arXiv:2412.03226* (2024).
 - [17] Y. Taur and T. H. Ning, *Fundamentals of modern VLSI devices* (Cambridge University Press, 2021).
 - [18] N. Freitas, J.-C. Delvenne, and M. Esposito, Stochastic thermodynamics of nonlinear electronic circuits: A realistic framework for computing around kT, *Physical Review X* **11**, 031064 (2021).
 - [19] C. Y. Gao and D. T. Limmer, Principles of low dissipation computing from a stochastic circuit model, *Physical Review Research* **3**, 033169 (2021).
 - [20] A. Gopal, *When nonlinear electronics meets thermal noise at the nanoscale: A stochastic thermodynamics approach*, Ph.D. thesis, University of Luxembourg (2024).
 - [21] P. Helms, S. W. Chen, and D. T. Limmer, Stochastic thermodynamic bounds on logical circuit operation,

- Physical Review E **111**, 034110 (2025).
- [22] G. Schrom and S. Selberherr, Ultra-low-power cmos technologies, in *1996 International Semiconductor Conference. 19th Edition. CAS'96 Proceedings*, Vol. 1 (IEEE, 1996) pp. 237–246.
 - [23] K. Kim, *Ultra low power CMOS design*, Ph.D. thesis, Auburn University (2011).
 - [24] C. Mead, Neuromorphic electronic systems, *Proceedings of the IEEE* **78**, 1629 (2002).
 - [25] V. Milo, G. Malavena, C. Monzio Compagnoni, and D. Ielmini, Memristive and cmos devices for neuromorphic computing, *Materials* **13**, 166 (2020).
 - [26] A. Jelinčič, O. Lockwood, A. Garlapati, G. Verdon, and T. McCourt, An efficient probabilistic hardware architecture for diffusion-like models, arXiv:2510.23972 (2025).
 - [27] R. J. Baker, *CMOS: circuit design, layout, and simulation* (John Wiley & Sons, 2019).
 - [28] B. Razavi, *Design of CMOS phase-locked loops: from circuit level to architecture level* (Cambridge University Press, 2020).
 - [29] M. Mandal and B. C. Sarkar, Ring oscillators: Characteristics and applications, *Indian Journal of Pure & Applied Physics* **48**, 136 (2010).
 - [30] A. Hajimiri, S. Limotyrakis, and T. H. Lee, Jitter and phase noise in ring oscillators, *IEEE Journal of Solid-state Circuits* **34**, 790 (2002).
 - [31] S. Robson, B. Leung, and G. Gong, Truly random number generator based on a ring oscillator utilizing last passage time, *IEEE Transactions on Circuits and Systems II: Express Briefs* **61**, 937 (2014).
 - [32] M. Bucci, L. Germani, R. Luzzi, A. Trifiletti, and M. Varanouovo, A high-speed oscillator-based truly random number source for cryptographic applications on a smart card IC, *IEEE transactions on computers* **52**, 403 (2003).
 - [33] B. Sunar, W. J. Martin, and D. R. Stinson, A provably secure true random number generator with built-in tolerance to active attacks, *IEEE Transactions on computers* **56**, 109 (2006).
 - [34] D. Liu, Z. Liu, L. Li, and X. Zou, A low-cost low-power ring oscillator-based truly random number generator for encryption on smart cards, *IEEE Transactions on Circuits and Systems II: Express Briefs* **63**, 608 (2016).
 - [35] Ü. Güler and G. Dündar, Modeling phase noise and jitter in subthreshold region and assessing the randomness performance of CMOS ring oscillators, in *2012 International Conference on Synthesis, Modeling, Analysis and Simulation Methods and Applications to Circuit Design (SMACD)* (IEEE, 2012) pp. 257–260.
 - [36] Ü. Güler and G. Dündar, Modeling CMOS ring oscillator performance as a randomness source, *IEEE Transactions on Circuits and Systems I: Regular Papers* **61**, 712 (2013).
 - [37] U. Seifert, Stochastic thermodynamics, fluctuation theorems and molecular machines, *Reports on progress in physics* **75**, 126001 (2012).
 - [38] C. Van den Broeck and M. Esposito, Ensemble and trajectory thermodynamics: A brief introduction, *Physica A: Statistical Mechanics and its Applications* **418**, 6 (2015).
 - [39] L. Peliti and S. Pigolotti, *Stochastic Thermodynamics: An Introduction* (Princeton University Press, 2021).
 - [40] A. Demir, A. Mehrotra, and J. Roychowdhury, Phase noise and timing jitter in oscillators, in *Proceedings of the IEEE 1998 Custom Integrated Circuits Conference (Cat. No. 98CH36143)* (IEEE, 1998) pp. 45–48.
 - [41] W. Vance and J. Ross, Fluctuations near limit cycles in chemical reaction systems, *The Journal of Chemical Physics* **105**, 479 (1996).
 - [42] P. Gaspard, The correlation time of mesoscopic chemical clocks, *The Journal of Chemical Physics* **117**, 8905 (2002).
 - [43] T. Xiao, J. Ma, Z. Hou, and H. Xin, Effects of internal noise in mesoscopic chemical systems near hopf bifurcation, *New Journal of Physics* **9**, 403 (2007).
 - [44] B. Remlein, V. Weissmann, and U. Seifert, Coherence of oscillations in the weak-noise limit, *Physical Review E* **105**, 064101 (2022).
 - [45] A. Gopal, M. Esposito, and N. Freitas, Large deviations theory for noisy nonlinear electronics: CMOS inverter as a case study, *Physical Review B* **106**, 155303 (2022).
 - [46] P. J. Davis, *Circulant Matrices*, Vol. 120 (Wiley New York, 1979).
 - [47] D. T. Gillespie, Exact stochastic simulation of coupled chemical reactions, *The Journal of Physical Chemistry* **81**, 2340 (1977).
 - [48] J. Guckenheimer and P. Holmes, Nonlinear oscillations, dynamical systems, and bifurcations of vector fields, *Applied Mathematical Sciences* **42** (1983).
 - [49] E. Ott, *Chaos in dynamical systems* (Cambridge University Press, 2002).
 - [50] G. Falasco and M. Esposito, Macroscopic stochastic thermodynamics, *Reviews of Modern Physics* **97**, 015002 (2025).
 - [51] For finite-size discrete systems, the analogue of \mathcal{L} is the so-called inflow rate [61], which converges to \mathcal{L} in the thermodynamic limit [11].
 - [52] C. W. Gardiner, *Handbook of stochastic methods for physics, chemistry and the natural sciences*, Springer Series in Synergetics (1985).
 - [53] N. Goldenfeld, *Lectures on phase transitions and the renormalization group* (CRC Press, 2018).
 - [54] Y. Cao, D. T. Gillespie, and L. R. Petzold, Adaptive explicit-implicit tau-leaping method with automatic tau selection, *The Journal of Chemical Physics* **126** (2007).
 - [55] A. C. Barato and U. Seifert, Cost and precision of Brownian clocks, *Physical Review X* **6**, 041053 (2016).
 - [56] D. Santolin and G. Falasco, Dissipation bounds the coherence of stochastic limit cycles, *Physical Review Letters* **135**, 057101 (2025).
 - [57] B. D. Sahoo, Ring oscillator based sub-1V leaky integrate-and-fire neuron circuit, in *2017 IEEE International Symposium on Circuits and Systems (ISCAS)* (IEEE, 2017) pp. 1–4.
 - [58] M. Rahaman Nayan and O. Hassan, Frequency tunable cmos ring oscillator-based Ising machine, *International Journal of Circuit Theory and Applications* **53**, 2958 (2025).
 - [59] Y. E. Gonul and B. Taskin, Multi-phase coupled CMOS ring oscillator based Potts machine, in *Proceedings of the 43rd IEEE/ACM International Conference on Computer-Aided Design* (2024) pp. 1–9.
 - [60] N. A. Aadit, A. Grimaldi, G. Finocchio, and K. Y. Cam-sari, Physics-inspired Ising computing with ring oscillator activated p-bits, in *2022 IEEE 22nd International Conference on Nanotechnology (NANO)* (IEEE, 2022) pp. 393–396.
 - [61] M. Baiesi and G. Falasco, Inflow rate, a time-symmetric

observable obeying fluctuation relations, Physical Review E **92**, 042162 (2015).